Deformation and failure kinetics of iPP polymorphs

Deformation and Failure Kinetics of iPP Polymorphs

H. J. M. Caelers,[1] E. Parodi,[1] D. Cavallo,[2] G. W. M. Peters,[1] L. E. Govaert[1,3]

[1]Department of Mechanical Engineering, Materials Technology Institute, Eindhoven University of Technology, P.O. Box 513, Eindhoven, MB 5600, the Netherlands
[2]Department of Chemistry and Industrial Chemistry, University of Genova, Via Dodecaneso 31, Genova, Italy
[3]Faculty of Engineering Technology, University of Twente, P.O. Box 217, Enschede, AE 7500, the Netherlands
Correspondence to: L. E. Govaert (E-mail: l.e.govaert@tue.nl)

Received 27 October 2016; accepted 13 January 2017; published online 00 Month 2017
DOI: 10.1002/polb.24325

ABSTRACT: In this study, the mechanical performance of the different polymorphs of isotactic polypropylene, typically present in iPP crystallized under industrial processing conditions, is assessed. Different preparation strategies were used to obtain samples consisting of almost solely α, β, or γ crystals. X-Ray measurements were used to validate that the desired phase was obtained. The intrinsic true stress - true strain response of all individual phases was measured in uniaxial compression at several strain rates (deformation kinetics). Moreover, measurements were performed over a wide temperature range, covering the window in between the glass transition and the melting temperature. The relation between obtained yield stress and the strain rate is described with a modification of the Ree-Eyring model. Differences and similarities in the deformation kinetics of the different phases are presented and discussed. Furthermore, the presence of three deformation processes, acting in parallel, is revealed. The Ree-Eyring equation enables lifetime prediction for given thermal and mechanical conditions. These predictions were experimentally validated using constant load tests in uniaxial compression. © 2017 Wiley Periodicals, Inc. J. Polym. Sci., Part B: Polym. Phys. **2017**, *00*, 000–000

KEYWORDS: α-, β- and γ-iPP; iPP-polymorphism; Mechanical behavior; Intrinsic properties; Yield kinetics; Lifetime predictions; Failure kinetics

INTRODUCTION Properties of isotactic polypropylene (iPP) result from a complex interplay between molecular architecture, strongly influenced by the polymerization method, additives, such as nucleating agents, and the morphological structure, which depends strongly on the thermo-mechanical history experienced during the solidification procedure. These "tools" create flexibility in tuning all kinds of properties, which is the main reason that iPP shows such a broad application range. One can for example tune the transparency by the addition of nucleating agent, which leads to smaller spherulites.[1,2] Toughness can be enhanced by the addition of a beta nucleation agent,[3] or the incorporation of a copolymer,[4] whereas elasticity and stiffness can be tuned with isotacticity.[5] A growing demand of iPP is currently found in structural applications, where temperature resistance and durability are key issues. The thermal stability can, for example, be improved by the addition of nanoparticles[6] and the long-term properties in the ductile failure regime improve with decreasing cooling rate.[7] For this demand of a variety of properties for all kinds of products, a detailed understanding of the underlying relations between structure and properties is of vital importance. When focusing at a fixed molecular architecture, in this case that of high tacticity iPP, one can still obtain huge differences in terms of crystal lattices and morphologies and, therewith, variation in physical and mechanical properties. Optimization of the properties by tuning the morphology with the applied conditions during the production process is a novel route towards improved performance, but, first, this requires knowledge about the structure–property relations. In this study, emphasis has been put on the effect of the crystallographic structure on the intrinsic mechanical response and the yield and failure kinetics. For isotactic polypropylene, it is common knowledge that, depending on the applied conditions during the crystallization process, multiple crystallographic structures can be formed.[8,9] If the isotacticity is sufficiently high, atmospheric pressure and moderate cooling conditions result in the formation of monoclinic α crystals, schematically shown in Figure 1(a). Low isotacticity or very high pressures result in orthorhombic γ crystals [Fig. 1(c)],[9–12] and the addition of β-specific nucleation agent or the application of high shear rates gives pseudo-hexagonal β unit cell structures; Figure 1(b).[8,13,14] Moreover, quenching iPP at high cooling rates leads to mesophase formation. This is enhanced with increasing stereoregularity[15] or propene/ethylene random copolymer content.[16] This mesomorphic form of iPP is a disordered crystalline form that shows long-range order only in the direction of the chain axis due to the ternary helical conformation. The cooling rates required to obtain almost solely mesophase in a high tacticity iPP are in the order of 200 °C/s.

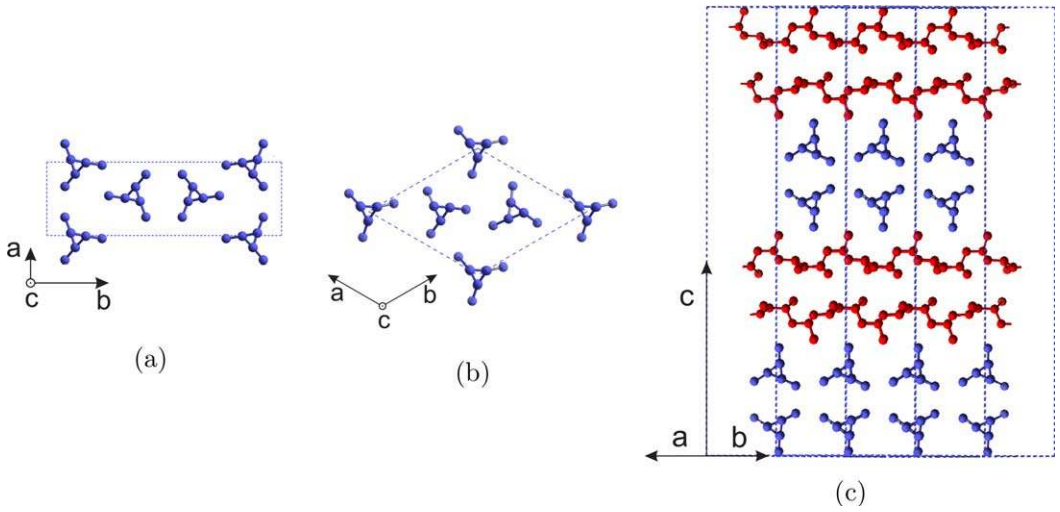

FIGURE 1 The crystallographic structures of the iPP-polymorphs. (a) Monoclinic α-iPP, (b) pseudo-hexagonal β-iPP, and (c) orthorhombic γ-iPP. [Color figure can be viewed at wileyonlinelibrary.com]

From a practical point of view, these conditions are difficult to fulfill and would result in large thermal and structural gradients when preparing samples for mechanical testing. Hence, the dimensions of tensile bars and of cylindrical samples used in tensile and compression experiments, respectively, have typically dimensions in the order of millimeters. Therefore, this form is not considered in this work.

The macroscopic behavior of iPP containing these structures has already been investigated extensively. For example, Van Erp et al. investigated the yield and failure kinetics of iPP materials containing either the dense α-phase or the less dense mesomorphic phase in uni-axial tensile deformation. Combinations of the two, in various compositions, were investigated and some remarkable similarities were found. The activation-energy and volume, required to describe the yield kinetics were the same for all compositions.[7] Lezak et al. studied the plastic deformation behavior in β-iPP at different temperatures in plane-strain compression[17,18] and made a comparison with α-iPP. The initial rate of strain hardening was found to be higher for the β-iPP. The explanation for this is that chain slip and plastic deformation is relatively easy in β crystals since no interlocking structures or cross-hatches are present, whereas they typically are, in the case of α-iPP. As a result, the hardening due to molecular and crystalline orientation takes place at lower strains.[19] The γ-iPP phase was also investigated by means of plane strain compression by Lezak et al.[17,20] It was found that the Young's modulus and the yield stress were much higher compared to the α crystals. Similar results were found in tensile deformation where the γ-form displays elastic behavior in a relatively large range of deformation.[21,22] These improved elastic properties in high tacticity iPP are thought to mainly originate from the fact that γ-iPP has a high fraction of tie chains (compared to α-iPP) that connect the crystalline domains and thus behave as stress transmitters.[23] Although the mechanical response of these crystal structures has been topic of many studies, an extensive investigation in which the focus is on both the yield kinetics and the failure kinetics, is still lacking. Moreover, according to the knowledge of the authors, similarities and differences in the kinetics measured over a broad range of temperatures and strain rates have not been reported so far.

The present study focuses on this topic and compares samples containing one of the individual crystal phases. The different protocols used to prepare the samples containing either α, β, or γ crystals will be discussed first. The results of the sample preparation are analyzed by means of X-ray. These samples are then used to reveal the intrinsic material response obtained from uniaxial compression experiments. The yield kinetics and the creep behavior are determined by performing experiments over a wide range of loading conditions. The findings are discussed separately and a model is presented that captures the results over the whole range of experimental conditions.

MATERIALS AND METHODS

Material

In this work, an isotactic polypropylene homopolymer from Sabic is used. The weight averaged molar mass M_w of this injection molding grade is 320 kg/mol with a polydispersity index M_w/M_n of 5.4. This iPP grade is synthesized with Ziegler–Natta catalyst and has a high tacticity.

Sample Preparation and X-Ray Characterization

In order to investigate the mechanical behavior of iPP containing almost solely one of the distinct crystal phases, different sample preparation procedures were used. X-Ray scattering is used to determine the degree of crystallinity and the lamellar thickness, which were measured by wide- and small-angle X-ray scattering (WAXD and SAXS) at the Dutch-Belgian (DUBBLE) beamline BM26B of the European Synchrotron and Radiation Facility in Grenoble (France)[24] using a Pilatus 300K and a Pilatus 1M detectors, respectively. The pixel size of both the detectors was 172 $\times$ 172 μm^2. In the case of the WAXD experiments, the detector was placed

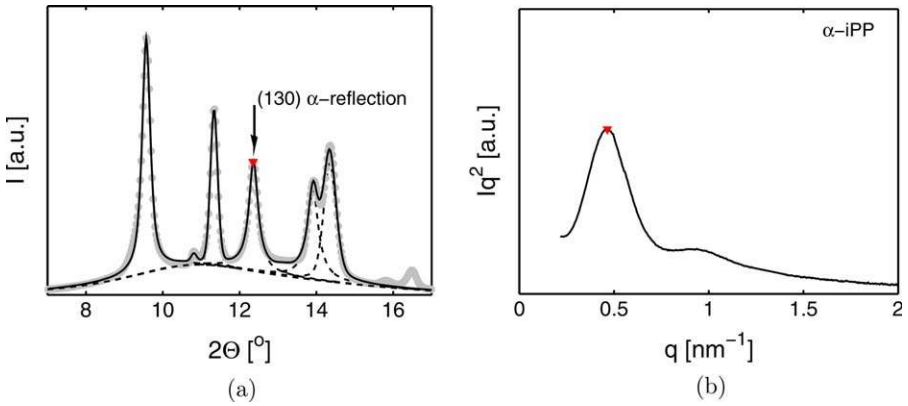

FIGURE 2 Radially integrated intensities as a function of the scattering angle 2θ (WAXD) and the Lorentz corrected scattering intensity as function of the scattering vector q (SAXS) for the α samples. The WAXD pattern is fitted using Voigt functions. The marker represents the characteristic reflection. The corresponding SAXS patterns are given in b). [Color figure can be viewed at wileyonlinelibrary.com]

at a distance of approximately 210 mm from the sample, whereas in case of the SAXS experiments, this distance was approximately 6470 mm. The wavelength of the X-ray beam was λ=1.033 Å. The exposure time was 30 s. All WAXD and SAXS data were background subtracted and integrated with the software package FIT2D. The intensity was plotted as a function of the scattering angle 2θ and the weight percentage of crystallinity followed from:

$$\chi_w = \frac{C_{tot} - C_a}{C_{tot}} \tag{1}$$

where C_{tot} is the total intensity (integrated area) and C_a is the integrated area of the scaled amorphous halo (determined on quenched low tacticity iPP with negligible crystallinity). The volume percentage of the crystallinity follows via:

$$\chi = \frac{\frac{\chi_w}{\rho_c}}{\frac{\chi_w}{\rho_c} + \frac{1-\chi_w}{\rho_a}} \tag{2}$$

where ρ_c and ρ_a are the density of the crystal phase and the amorphous phase, respectively. The WAXD pattern was then used to determine the phase content of the desired crystal structures by means of fitting of the diffraction peaks using Voigt functions. To determine the long period from the SAXS data, the Lorentz corrected intensity was plotted as a function of the scattering vector q, given by:

$$q = \frac{4\pi}{\lambda}\sin(\theta) \tag{3}$$

where λ is the wavelength and θ is half the scattering angle. For an isotropic system with a randomly oriented lamellar morphology, the scattered intensity can be transposed to a 1D intensity using the Lorentz correction:

$$I_1(q) = I(q)q^2 \tag{4}$$

After the correction, the long period and lamellar thickness can be obtained from:

$$l_c = l_p \cdot \chi = \frac{2\pi}{q_{I_1,max}}\chi \tag{5}$$

where $q_{I_1,max}$ is the value for the magnitude of the scattering vector, corresponding to the maximum of the Lorentz corrected intensity.

α-Crystals

Plates with a thickness of 6 mm containing α-iPP were prepared using compression molding. The mold was placed in between a stack of aluminum foil (0.2 mm) and stainless steel plates (3 mm), and subsequently placed in a hot press at a temperature of 230 °C. Once the polymer was in the melt, pressure was applied stepwise until it reached a final value of about 10 MPa. The sample was kept at this temperature for 5 min, erasing thermal history, and subsequently placed in a cold press at 20 °C. After solidification, the sample was removed from the mold. Cylindrically shaped compression specimens with a diameter and a height of Ø4 × 4 mm^2 were machined from the plates, stored at room temperature, and used in uniaxial compression experiments about 1 month after sample preparation. Sample characterization was done by means of WAXD and SAXS experiments. In Figure 2(a), the result of a radial integration on the α-iPP pattern is shown. The characteristic α reflection at $d = 4.78$Å ($2\theta = 12.4°$) is marked red. The reflections of β and γ crystals are very small and can be found at $d = 5.50$Å ($2\theta = 10.83°$) and $d = 4.38$Å ($2\theta = 13.31°$), respectively. After fitting the amorphous halo, the volume percentage of crystals χ was determined via (eq 2) to be 60%. Further fitting of the X-ray signal allows us to calculate the percentage of α crystals in the sample according to:

$$\chi_\alpha = \frac{A_\alpha}{A_\alpha + A_\beta + A_\gamma} \tag{6}$$

where χ_α is the volume fraction of α crystals and A_i is the area of the Voigt function that was used for fitting, corresponding to the different crystal structures. From this, it was

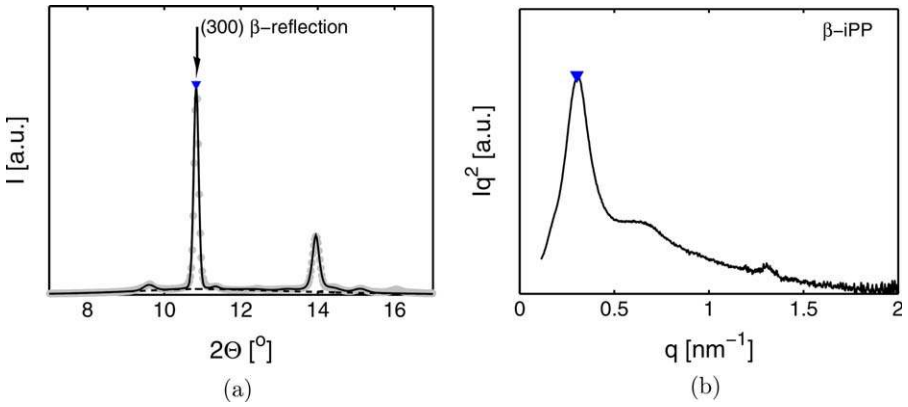

FIGURE 3 Radially integrated intensities as a function of the scattering angle 2θ (WAXD) and the Lorentz corrected scattering intensity as function of the scattering vector q (SAXS) for the β samples. The WAXD pattern is fitted using Voigt functions. The marker represents the characteristic reflection. The corresponding SAXS patterns are given in b). [Color figure can be viewed at wileyonlinelibrary.com]

found that a successful procedure was used to prepare samples containing mainly the α-phase with a volume percentage of approximately 94%. The lamellar thickness is obtained from the Lorentz corrected radially integrated SAXS experiments, shown in Figure 2(b), and the WAXD data using (eq 5). The average crystal thickness L_c is found to be 8.2 nm.

β-Crystals

To study the deformation and failure kinetics of the β-phase iPP, a specific nucleating agent, NJSTAR NU100 (New Japan Chemical Group), was added with a weight percentage of 0.1% using a twin skrew extruder. The β nucleated iPP pellets were compression molded in a mold of 8 mm thickness. The procedure of the melting, the stepwise application of the pressure and the solidification was the same as for the α-iPP. The diameter and height of the cylindrical samples for the uniaxial compression experiments were Ø6 $\times$ 6 mm^2.

The fitting of the integrated WAXD pattern, see Figure 3(a), was again done with Voigt functions after subtraction of the amorphous halo. The crystallinity of the β-iPP was determined at 64 volume % of which 95% was the actual pseudo-hexagonal β-phase. The long period and the lamellar thickness are larger than in case of the α-iPP (20.8 and 13.3 nm, respectively). This follows directly from the SAXS result since the crystallinity is about the same, Figure 3(b).

γ-Crystals

To prepare iPP containing mainly γ-crystals, a device is required that enables us to apply pressures high enough for the formation of orthorhombic structures. From Mezghani et al.,[10] it is known that isothermal crystallization of high isotacticity iPP, like the one used in this work, requires a pressure of 180 MPa and a crystallization temperature around 180 °C. This isothermal crystallization under these conditions predominantly results in the formation of γ-crystals. For this reason, a special tool was designed, enabling us to apply these conditions during solidification.

In Figure 4, a schematic of the pressure cell and a picture of the setup is shown. The device basically consists of a hollow cylinder containing cooling channels and heating elements. From bottom and top, two plungers with a diameter of 60 mm, sealed with teflon plates, are used to apply pressure on the polymer. With the integrated cooling channels, the applicable cooling rate is maximized and, therefore, the required time to reach the isothermal crystallization conditions is reduced. To control the temperature, thermocouples and heating elements are placed not only in the cylinder, but also in both the plungers, as close to the sample as possible. The pressure is controlled manually using a jack. The sample preparation procedure is designed on the basis of the work of Mezghani et al.,[10] and shown in Figure 4(c), where the applied thermo-mechanical history is shown as a function of time. The temperature is first increased to melt the iPP granulate. After erasing thermo-mechanical history and removing the trapped air, a pressure of 180 MPa is applied. Next, the sample is kept under isothermal conditions at 178 °C, which is sufficiently low to crystallize the material (The melting temperature increases approximately 30 °C when the pressure is increased 100 MPa, and with that also the undercooling[25]). Finally, when the crystallization process has finished, the sample is cooled to room temperature by blowing compressed air through the cooling channels. After reaching room temperature, the pressure is released and cylindrical disks containing γ-iPP are obtained. As a result, multiple compression samples of Ø6 $\times$ 6 mm^2 can be machined from 1 crystallization cycle. The WAXD pattern of the γ-iPP is shown in Figure 5(a). With fitting, the γ phase content is found to be 99% of the total crystal fraction χ, determined at 67%, meaning that the used procedure resulted in almost solely γ-crystals with an average lamellar thickness L_c of 10.0 nm. The SAXS pattern is shown in Figure 5(b) and a summary of the sample characteristics is given in Table 1.

DMTA

DMTA measurements were performed on a TA Instruments Q800. Rectangular samples of 1 mm $\times$ 4.5 mm $\times$ 30 mm (t $\times$ w $\times$ l), containg α, β, and γ crystals were machined from the polymer sheets. A frequency of 1Hz in a strain-controlled experiment with an amplitude of 5 μm/mm was applied.

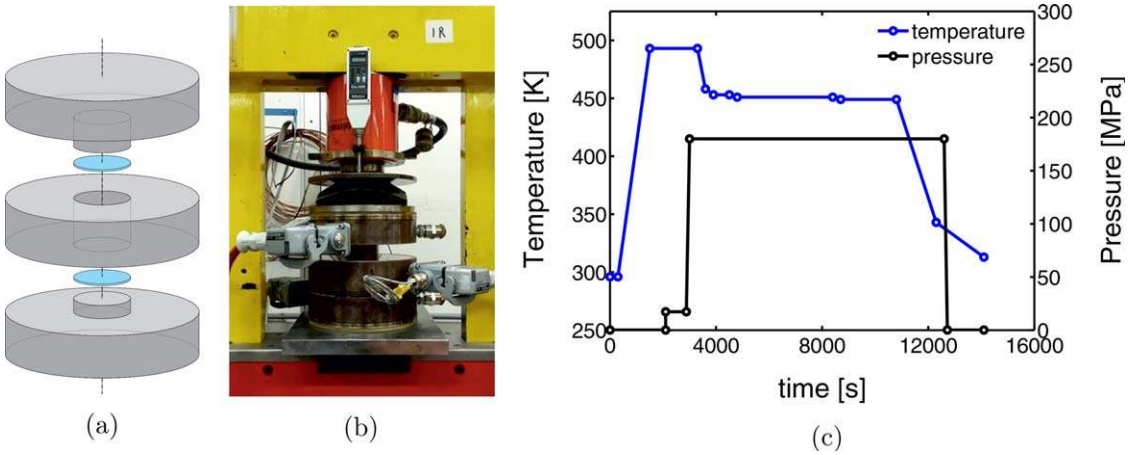

FIGURE 4 (a) Schematic of the tool that is used apply pressures to prepare iPP with γ-crystals. The blue disks are teflon plates for sealing. (b) A picture of the experimental setup. (c) The pressure-temperature protocol to prepare γ-iPP. [Color figure can be viewed at wileyonlinelibrary.com]

The storage and loss modulus were measured in a temperature window ranging from −80 to 150 °C.

Mechanical Testing

The mechanical characterization was done with uniaxial compression experiments performed on a Zwick 1475, equipped with a load cell of 100kN and a temperature chamber. Contact resistance between the cylindrically shaped specimens and the compression setup was reduced as far as possible with PTFE tape (3M 5480) on the flat side of the cylinder. Additionally, the contacts between the tape and the compression plates were lubricated with PTFE spray (Griffon TF89). Constant true strain-rate experiments were performed at rates of 10^{-5} to 10^{-1} s^{-1} and temperatures from −10 to 110 °C in true strain control. In addition, the time to failure was measured using creep experiments in which constant true stress was applied. In both the type of experiments, a correction was made in the true strain calculation to account for the stiffness of the experimental setup. Before starting the compression tests, the samples were stored at the test temperature for 10 min to obtain thermal equilibrium between the sample and the thermally controlled environment in the oven.

RESULTS AND DISCUSSION

First, the mechanical behavior is compared in terms of DMTA measurements. Next, the intrinsic material behavior of iPP containing almost solely α, β, or γ crystals is discussed and compared by looking at the true stress - true strain response following from uniaxial compression experiments at room temperature and a strain rate of 10^{-3} s^{-1}. Finally, the comparison is extended to the yield and failure kinetics, that is, the yield and failure behavior over a broad range of temperatures and strain rates.

DMTA

The storage (E') and loss (E'') moduli measured on the three iPP samples are given in Figure 6(a). Both the elastic and viscous moduli show qualitatively similar behavior in the lower temperature range. However, at temperatures between 40 and 120 °C, the β-iPP shows a clear discrepancy when

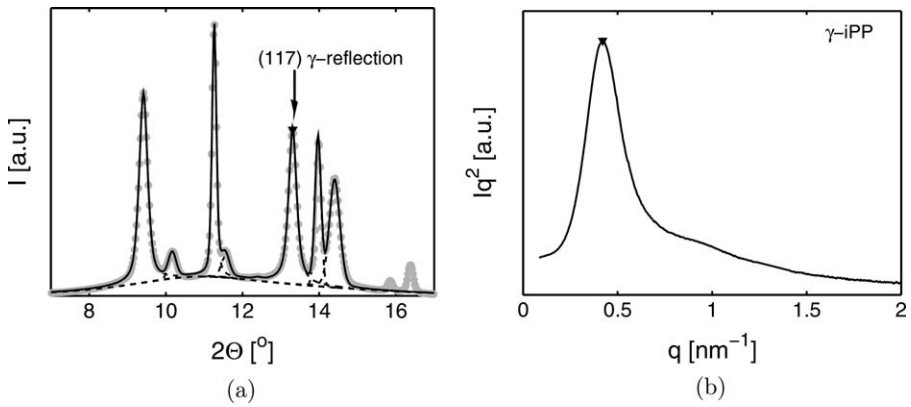

FIGURE 5 Radially integrated intensities as a function of the scattering angle 2θ (WAXD) and the Lorentz corrected scattering intensity as function of the scattering vector q (SAXS) for the γ samples. The WAXD pattern is "fitted" using Voigt functions. The marker represents the characteristic reflection. The corresponding SAXS patterns are given in b).

TABLE 1 Sample Preparation and Resulting Crystallinity (χ_w and χ), long period L_p, lamellar thickness L_c, and amorphous layer thickness L_a

	α-iPP	β-iPP	γ-iPP
χ_w weight %	63	66	69
χ volume %	60	64	67
L_p [nm]	13.5	20.8	14.9
L_c [nm]	8.2	13.3	10.0
L_a [nm]	5.3	7.5	4.9

comparing with the other two samples. This is reflected in the DMTA experiments performed on these samples, as is shown in Figure 6(b), where the relaxation mechanism in β-iPP appears less pronounced. Here, the $tan(\delta)$ and the dynamic modulus E_d as a function of temperature are shown. In the $tan(\delta)$ curve characteristic material behavior can be recognized and interpreted.

From the classical work performed by Boyd,[26] it is known that when going from high to low temperatures the first peak, the α_c relaxation, can be found around 90 °C. This mechanism is related to rearrangements of/on the crystal surface due to translational movement of the stems. These movements can lead to redistributions of tight and loose folds and the intercrystalline links and, therefore, softening of the interlamellar material. The second peak, around a temperature of 15 °C, is assigned to the β relaxation or the α_a relaxation. The relaxation mechanism is linked to the loss of mobility in the (bulk) amorphous phase and is similar to the glass transition in an amorphous polymer. Finally, the last peak at a temperature of about −40 °C can be attributed to the γ relaxation. This relaxation mechanism is linked to the loss of segmental mobility in the (bulk) amorphous phase. All iPP samples exhibit the expected response, but in the case of β-iPP, the α_c transition is smeared out over a much broader temperature range than for the other two samples. The peak position of the α_a relaxation is about the same for all iPP samples. The dynamic moduli, also shown in Figure 6(b), reveal that the γ-iPP displays the highest modulus over almost the entire temperature range. At low temperatures, the α-iPP has a much lower modulus.

An important observation for the case of iPP is that the moduli in the α_a and the α_c relaxation regions are not a unique function of the crystallinity.[26] The variation of the moduli with the crystallinity depends on how the crystals have been created. Furthermore, the α_a relaxation is related to the mobile amorphous fraction (MAF) in iPP, which can change upon storage at room temperature,[27] see also Yield Kinetics section. In DMTA experiments, the amount of MAF is reflected in the area of the α_a relaxation peak.[28] With an increasing fraction of MAF, the peak area increases. Simultaneously, the area underneath the α_c relaxation peak reflects the amount of rigid amorphous fraction (RAF). In a qualitative way, it can immediately be observed that the β-iPP displays a different response, particularly in the temperature window of the α_c relaxation, indicating that the amount of RAF is much smaller than in the case of the α- and γ-iPP. The amount MAF on the other hand is the largest for β-iPP (hence, the logarithmic scale). This observation is confirmed by the work of Policianova et al.,[29] where solid-state NMR was used to investigate the molecular mobility in the amorphous and crystalline domains of α and β-iPP. Compared to β-crystals, the α-crystals exhibit larger restrictions on the chain mobility in the crystals, as well as in the constrained amorphous domains. Based on the DMTA results, it is expected that the RAF in γ-iPP is even more constrained.

Intrinsic Material Response

To investigate the intrinsic stress-strain response, that is, the material behavior in homogeneous deformation (to eliminate effects of sample geometry), the mechanical behavior is studied by means of uniaxial compression experiments. A typical example of results obtained from such experiments is shown in Figure 7, where the response, measured at room

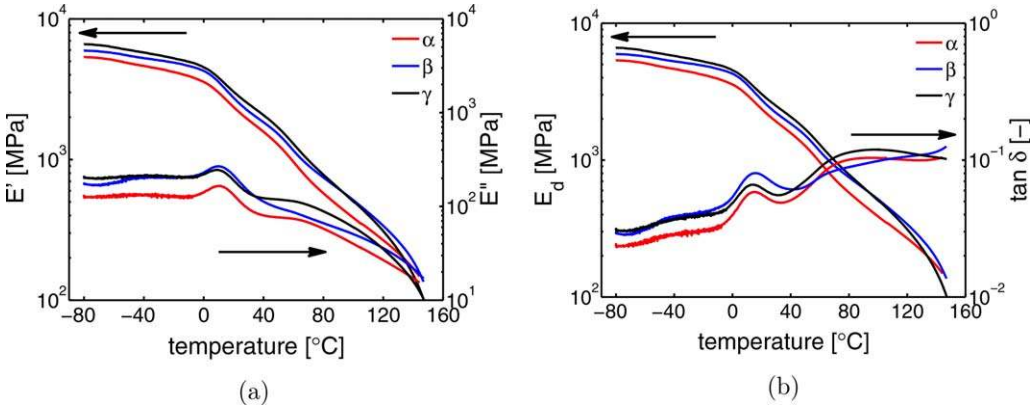

FIGURE 6 (a) The elastic and storage modulus of the iPP polymorphs as a function of temperature and (b) the dynamic modulus and the $tan(\delta)$ as a function of the temperature. The dynamic modulus E_d is the lowest for α-iPP and the highest for γ-iPP in almost the entire temperature window. The α_c relaxation of β-iPP is smeared out over a much broader transition range compared to α-iPP and γ-iPP. [Color figure can be viewed at wileyonlinelibrary.com]

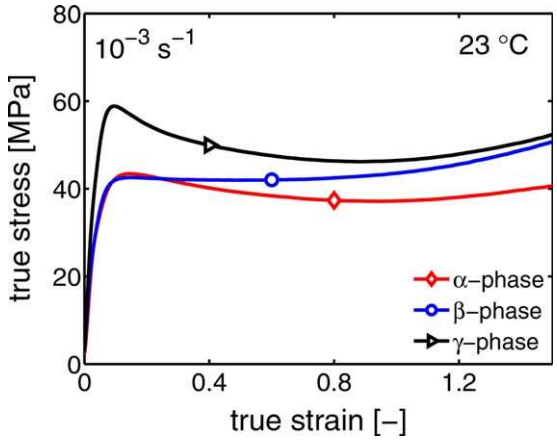

FIGURE 7 Intrinsic stress–strain response in uniaxial compression experiments, measured at room temperature and a strain rate of 10^{-3} s^{-1}. [Color figure can be viewed at wileyonlinelibrary.com]

temperature and a strain rate of 10^{-3} s^{-1}, of α-, β-, and γ-iPP is shown. Initially linear elastic behavior is displayed but with increasing strain, and consequently increasing stress, a growing deviation from this behavior can be observed. The increasing stress makes the system more mobile, and thereby facilitates plastic deformation. At the yield stress, the mobility has become that high that the plastic deformation rate equals the applied strain rate. A higher applied strain rate requires a higher stress to achieve this balance for yielding, giving rise to the rate dependency of the yield stress. Mobility is also facilitated by temperature, making plastic flow more easily at elevated temperatures. After yielding, softening can be observed, subsequently followed by hardening. Obviously, these mechanical characteristics are strongly connected to the morphology and structure on a microscopic scale. In the following sections, we elaborate on the structural features that are of importance for these properties, and make a comparison between the different crystal structures.

Elastic Modulus

The elastic modulus is taken from the slope of the stress–strain response in the region were the behavior is linear elastic. The moduli show a strong temperature, see Figure 8, and rate dependence, originating from the time-dependent nature of polymeric materials. Determination of the modulus between true strains of 0.4 and 1% reveals that the value of the modulus is the highest for the γ crystals and the lowest for the α crystals. As expected, this is correlated to the crystallinity of the samples, Table 1. However, another contributing factor to the Young's modulus is the part of the amorphous phase that is in the glassy state at a given temperature. Besides crystallinity, the constraints imposed by the different crystallographic structures also affect the elastic modulus. The trend is in good agreement with the complex modulus measured with DMTA and plotted in Figure 6(b).

Yield Stress

The yield stress of polymers depends strongly on loading conditions and, in the case of semicrystalline polymers, it depends on structural features like crystallinity or lamellar thickness as well.[7] Furthermore, imperfections in the crystal lattices can have a pronounced effect.[30] It is difficult to draw clear conclusions on the effect of these distinct structural features, since it is hard to vary single features without affecting others. The crystallinity of the α, β, and γ-iPP studied in this work is quite similar, but differences are present in, for example, the lamellar thickness. Moreover, the amount of imperfections in the crystals cannot be easily quantified. Although the crystallinities are comparable, the γ-samples show a much higher yield stress than β and α-iPP, see Figure 7. The lamellar thickness of α-iPP is much smaller than the lamellar thickness of β-iPP, but the yield stress is similar. This illustrates the before mentioned difficulties. For a given crystal phase, the yield stress is correlated to the lamellar thickness; an increase of about 2 nm in the lamellar thickness of α -IPP yields an increase of approximately 8 MPa in the yield stress.[31] This gives rise to the presumption that an additional feature like the crystal unit cell structure or the accompanying amount of imperfections affects the level of the yield stress as well. In Yield Kinetics section, we give a possible explanation for the large differences in the yield stress of the γ-phase compared to α and β -iPP, based on the fact that in deformation at least half of the chains in the γ crystals is loaded under an angle. The amorphous layer thickness and the constraints applied by the crystals on the amorphous domains most likely affects the level of the yield stress, as was already observed in the DMTA experiments.

Strain Softening

In the amorphous phase, physical aging results in an increase in the yield stress. Upon deformation, the stress decreases and, therefore, mechanically rejuvenates the sample. This process is called softening and is also observed in α and γ-iPP (Fig. 7). The glass transition temperature T_g of

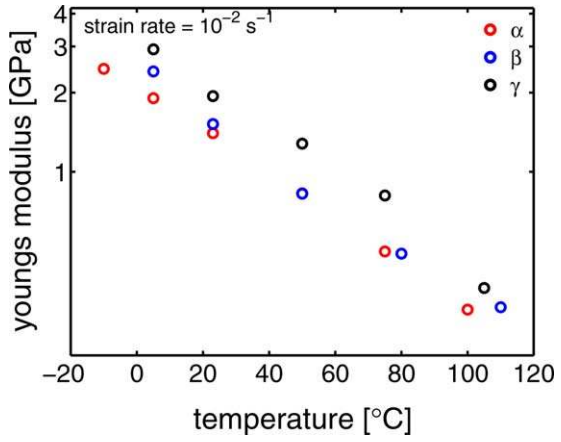

FIGURE 8 The Young's moduli obtained from uniaxial compression experiments at a strain rate of 10^{-2} s^{-1} at different temperatures for the three iPP polymorphs. [Color figure can be viewed at wileyonlinelibrary.com]

bulk amorphous iPP is about −10 °C and is therefore lower than the temperature employed in the experiments. However, the transition from crystalline toward amorphous domains is not sharp. In the vicinity of the crystals, the amorphous phase is constrained and thus less mobile. This leads to a gradient in the glass transition temperature. As a result, parts of the amorphous domains can be in the glassy state, even at temperatures far above the bulk amorphous T_g. For example, at room temperature, in the specific case of iPP, a distinction can be made between mobile amorphous domains and rigid glassy amorphous domains. These domains are possible contributors to the softening behavior observed in the true stress–true strain response, depending on the temperature. Moreover, the amount of softening varies with the thermodynamic state and the fraction of the rigid amorphous phase. Besides the amorphous contribution to softening, there can also be a crystalline contribution. Yielding or plastic flow induces the destruction of crystals at low temperatures or phase transitions at elevated temperatures. Especially, the destruction of crystals is generally accompanied by a decrease in the resistance against deformation (softening) and, therefore, a reduction of the stress in a constant rate experiment. The level of destruction is governed by the mobility of the chains within the crystallographic structure which is connected to the density. A comparison between the softening of α, β, and γ-iPP, Figure 7, reveals tremendous differences. Where the β-crystals do not show softening in their stress–strain response, the γ crystals display a yield drop of about 15 MPa and the α-crystals are in between.

Strain Hardening

In Figure 7, it can be seen that β-iPP shows much stronger strain hardening than α-iPP. The hardening of γ-iPP samples is slightly stronger then that of α-iPP. In general the level of hardening is assigned to the network density, which is high for γ-iPP.[32] In the case of semi-crystalline polymers this density consists out of entanglements and tie-molecules, since both can act as stress transmitters.

The entanglement density is related to the chain stiffness. Since in this work all samples are prepared with the same polymer this can not explain the large differences observed in the experiments. From Schrauwen et al.,[33] it is known that within the exact same polymer, different hardening moduli can be found. This observation was attributed to reeling in; rearrangement of polymer chains that are folded into the crystals. In the case of β iPP, nucleating agent is used and therefore the crystallization kinetics are very fast, reducing this phenomenon.[34] The γ-iPP on the other hand is isothermally crystallized, allowing in theory for chains reeling in and thus more disentanglement of the amorphous phase. Observing significant differences in the hardening modulus caused by reeling in requires much larger differences crystallization times. Indeed, the time scales used by Schrauwen et al. to investigate reeling-in were much higher than the time scales required for the sample preparation in this work, taking this effect as an explanation for differences between the hardening of α-, β-, and γ-iPP into question.

After yielding and plastic flow, chains can move through the crystals and therefore tie molecules loose their ability to act as a stress transmitter. However, it is known that upon deformation the solid state phase transitions take place into either meso-phase or other crystal structures.[17,18,20,21,35–37] This means that the structural integrity is at least partially maintained, and the destruction, transformation or reformation of crystals upon the application of strain can in that perspective no longer be neglected. To reveal the exact role of the different mechanisms and find out wether they explain the large differences in hardening, further research is required.

Yield Kinetics

The intrinsic yield kinetics are investigated by means of compression tests of which the results are shown in Figure 9, where the true stress as a function of the true strain is plotted for some of these experiments. The markers indicate the yield stress, defined as the maximum. Occasionally, in the case of β-iPP, a well defined yield point is missing. In these cases the yield stress was defined as the true stress corresponding to a true strain of 0.16 [-], which is chosen since this is a strain at which yielding typically occurs.

First, we will focus on the yield kinetics of α-iPP to discuss the typical behavior and the dependence on the loading conditions, that is, temperature and strain rate. When plotting the yield stress as a function of the applied strain rate [Fig. 10(a)], it can be observed that at room temperature the rate dependency is much stronger than at elevated temperatures. This typical behavior is observed for many polymeric systems, either amorphous[38] or semi-crystalline[39] and the presence of multiple rate dependencies is related to the different deformation mechanisms that are active.

A successful way to describe this behavior was proposed by Ree and Eyring,[40] who modeled the different rate dependencies by two stress activated deformation processes acting in parallel according to eq 7:

$$\sigma_{\text{total}} = \sum_i \sigma_i = \sum_i \frac{kT}{V_i^*} \sinh^{-1}\left(\frac{\dot{\epsilon}}{\dot{\epsilon}_{0,i}\exp(-\Delta U_i/RT)}\right), \quad (7)$$

where k is the Boltzman constant, R is the universal gas constant, T is the temperature in [K], $\dot{\epsilon}$ is the applied strain rate, V_i^* is the activation volume of deformation mechanism i, ΔU_i is the activation energy of mechanism I, and $\dot{\epsilon}_{0,i}$ is the rate constant. In this study, however, the experimentally assessed temperature window is extended so that a third deformation mechanism is required to adequately describe the yield kinetics.

Using this equation to fit the experimentally obtained yield stress for α-iPP results in the description shown in Figure 10(a).

The same fits are made for β- and γ-iPP shown in Figure 10(c,e), respectively. At room temperature the rate dependence of the γ-iPP is clearly the strongest and the yield stress is about 20% higher than in case of the α or β-iPP. This is partly due to the fact that for γ-iPP, the contribution of the third-rate

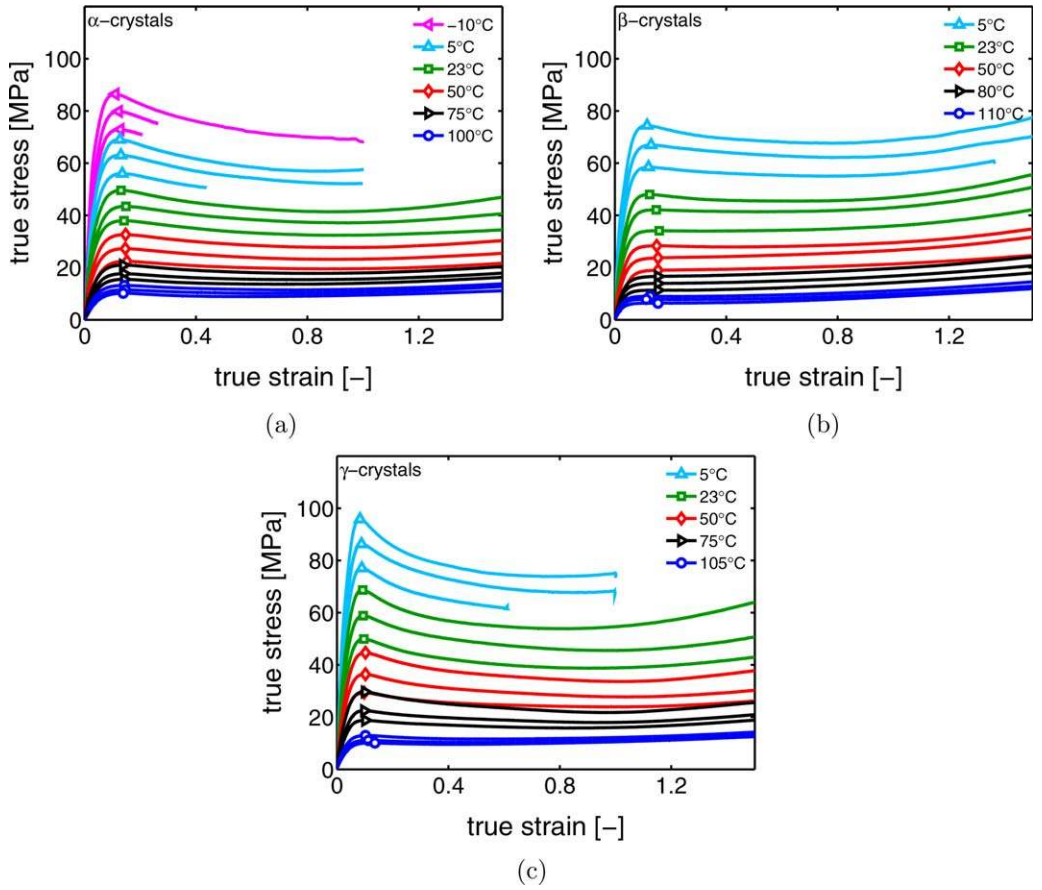

FIGURE 9 (a) The stress–strain response of α-iPP for different strain rates and temperatures. The temperature range varies between a minimum temperature around the glass transition and a maximum well below the melting temperature of the crystals. The strain rates shown in the graphs are 10^{-4}, 10^{-3}, and 10^{-2} from bottom to top. (b) The stress–strain response of β-iPP and (c) the stress–strain response of γ-iPP. The markers represent the yield stress. [Color figure can be viewed at wileyonlinelibrary.com]

dependency can already be observed in the response at room temperature [This is more clear in Fig. 10(b,d,f)].

In the case of α-iPP the appearance of a third slope is less obvious than in the case of γ-iPP, when only looking at the rate dependency. For this reason, the yield data are presented in a different way, see Figure 10(b,d,f), where the yield stress is plotted as a function of the temperature for different strain rates. From this figure, it is very obvious that the temperature dependency displays three different regions, each with their own slope.

The parameters used to describe the yield data are given in Table 2 for all crystallographic structures and the three deformation mechanisms. The activation volume is a measure for the rate dependency, whereas the activation energy is directly related to the temperature dependence. The rate constants are state parameters and depend on for example the lamellar thickness or physical age of the rigid amorphous domains.[7] Variations in the rate constants are only meaningful if the activation energy and volume are kept constant. For that reason they are not discussed further in this section, where the values of the Eyring parameters (for the different crystal structures) are compared.

The presence of the additional third deformation mechanism has already been observed before,[41,42] and for the interpretation we start from Figure 10. Here, it can be clearly observed that for all three polymorphs the yield stress contribution of process 2 becomes negligible at a temperature of 80 °C and a strain rate in the order of 10^{-2}–10^{-3} s^{-1}. This implies that, at higher temperature or lower strain rates, there is sufficient thermal mobility to facilitate the molecular deformation process without the requirement of substantial stress activation. The DMTA results in Figure 6 indicate that this "fade-out" region of the deformation mechanism II contribution coincides well with the onset of the so-called α_c-relaxation. This transition finds its origin in the migration of conformational defects within the crystalline phase, causing a translational mobility of chains throughout the crystal lattice (chain diffusion).[26,43] This chain mobility releases the constraint on the inter lamellar amorphous region, allowing it to relax and deform. This creates the peculiar situation that the relaxation strength of the α_c-transition is linked to the interlamellar amorphous regions, whereas the mobility undoubtedly originates within the crystalline phase.[26] In the case of the α and β-polymorphs, the activation energy for process II, 195 kJ/mol, is well within

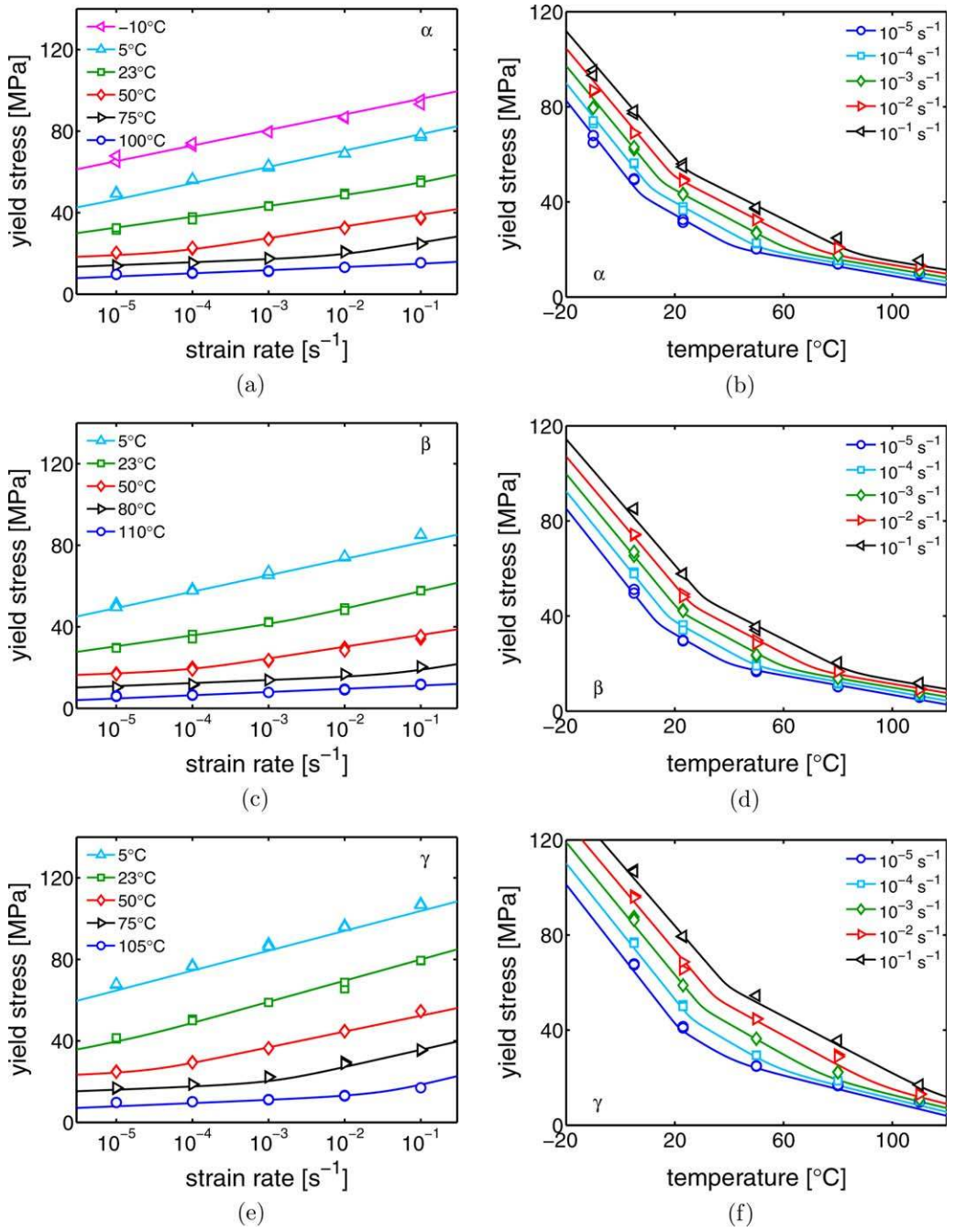

FIGURE 10 The yield kinetics of (a) α-iPP, (c) β-iPP, and (e) γ-iPP. Markers represent the yield stress found with uniaxial compression experiments and lines are best fits of eq 7. The yield kinetics of (b) α-iPP, (d) β-iPP, and (f) γ-iPP presented as a function of temperature. Again, lines are descriptions using the Eyring theory and markers represent the experimentally obtained yield stress. [Color figure can be viewed at wileyonlinelibrary.com]

the range of 163-222 *kJ/mol* reported for α_c-relaxation in literature.[44,45] It seems therefore appropriate to assign process II to deformation of the inter lamellar amorphous regions. Remarkably, the value for the γ polymorph is considerably lower with only 125 kJ/mol. To our knowledge, however, there are no previous reports for α_c-relaxation in γ-iPP. A hypothesis for the large differences observed between γ-iPP and the other crystal structures is given later in this section.

Concerning the high temperature/low strain rate process I, plastic deformation of the crystalline lamellae through a crystallographic slip mechanism was previously proposed as the underlying mechanism.[30,46–48] Remarkably, however, the results presented here for the different polymorphs seem to disagree with this interpretation. As presented in Figure 1, the crystalline unit cells are considerably different for the three polymorphs, and, consequently, it is difficult to imagine

TABLE 2 List of Parameter Values

	V_i^* [m^3]	ΔU_i [J·mol^{-1}]	$\dot{\epsilon}_{0,i}$ [s^{-1}]
α-Crystals			
Mechanism *I*	$7.70 \cdot 10^{-27}$	$3.84 \cdot 10^5$	$2.0 \cdot 10^{43}$
Mechanism *II*	$2.31 \cdot 10^{-27}$	$1.95 \cdot 10^5$	$4.1 \cdot 10^{27}$
Mechanism *III*	$2.89 \cdot 10^{-27}$	$3.95 \cdot 10^5$	$6.5 \cdot 10^{68}$
β-Crystals			
Mechanism *I*	$7.70 \cdot 10^{-27}$	$3.84 \cdot 10^5$	$4.2 \cdot 10^{44}$
Mechanism *II*	$2.31 \cdot 10^{-27}$	$1.95 \cdot 10^5$	$5.9 \cdot 10^{27}$
Mechanism *III*	$2.89 \cdot 10^{-27}$	$3.95 \cdot 10^5$	$1.6 \cdot 10^{67}$
γ-Crystals			
Mechanism *I*	$7.70 \cdot 10^{-27}$	$5.30 \cdot 10^5$	$2.0 \cdot 10^{63}$
Mechanism *II*	$1.59 \cdot 10^{-27}$	$1.25 \cdot 10^5$	$9.6 \cdot 10^{15}$
Mechanism *III*	$2.89 \cdot 10^{-27}$	$3.95 \cdot 10^5$	$2.0 \cdot 10^{65}$

that the slip kinetics of the polymorphs would be comparable. Nevertheless, the deformation kinetics (in terms of activation volume and thus stress dependence) are nearly identical for all three crystallographic structures. An explanation for this observation can possibly be found in the fact that the only structural similarity between the three crystallographic structures is the presence of isotactic chains in a ternary helical conformation. Since, above the α_c-relaxation temperature, or at appropriate time scales, these chains will have obtained translational mobility, the origin of the plastic deformation of the lamellae might be found in a collective diffusive mobility of the chains from which the crystal is comprised. This collective translational mobility renders the crystal "fluid-like", giving rise to a diffuse type of deformation that is quite distinct from crystallographic slip.[49]

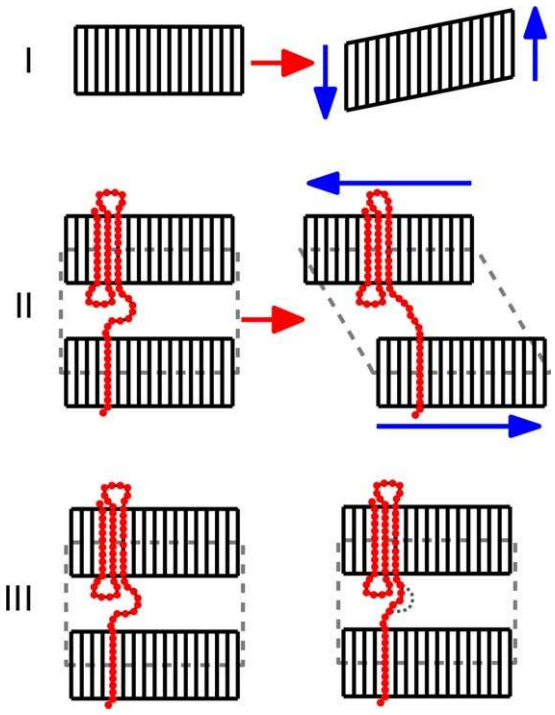

FIGURE 11 A schematic representation of the structure prior to deformation and after intra lamellar deformation or crystal slip (mechanism I), interlamellar or α_c relaxation (mechanism II) and β or α_a relaxation (mechanism III). [Color figure can be viewed at wileyonlinelibrary.com]

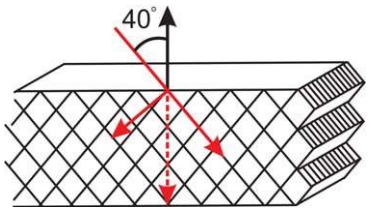

FIGURE 12 A schematic representation of iPP chains in γ lamellae. The force applied perpendicular to the lamellar stack can be decomposed in components parallel to the chain. [Color figure can be viewed at wileyonlinelibrary.com]

The third process, appearing at low temperatures or high strain rate appears to be linked to the low temperature transition observed in DMTA, generally assigned to the glass transition of the unconstrained amorphous phase. For all three crystallographic structures the activation energy and activation volume of this α_a-relaxation (or β-relaxation) is identical. The yield kinetics in the low temperature region are not influenced by the crystals and as expected, the Eyring parameters are similar, independent of the crystal structures.

A schematic interpretation of these three different mechanisms follows from the classical work of Boyd,[26] and is depicted in Figure 11.

Considering this schematic representation, combined with the observations made for the intra-lamellar deformation mechanism I, a discussion is triggered to find an explanation for the difference in activation energy between γ-iPP and the other two polymorphs. First of all, this mechanism is interpreted as a diffuse type of deformation, rather than the slip of planes within the crystallographic structure itself. Therefore it is suggested that the mobility of the helix is the dominant factor to determine the stress and temperature dependence of this process. However, as mentioned before, the activation energy for the α and β-iPP can be chosen the same, whereas the activation energy of γ-iPP is distinctly higher. This activation energy of the intra-lamellar deformation mechanism is not related to the amount of imperfections in the crystals or the lamellar thickness, since both can be modeled successfully by only varying the rate constant, as is shown by Pepels et al.[30] and van Erp et al.[7] respectively. Therefore this can not be an explanation for the huge difference in activation energy observed for γ-iPP. On the other hand, it is known that γ crystals display a crossed stacking of the chains within the lamellae, see Figure 12. This might possibly be at the origin of the high activation energy and yield stress. Due to the chain packing within the crystal lattice, stresses arising upon deformation always act under an

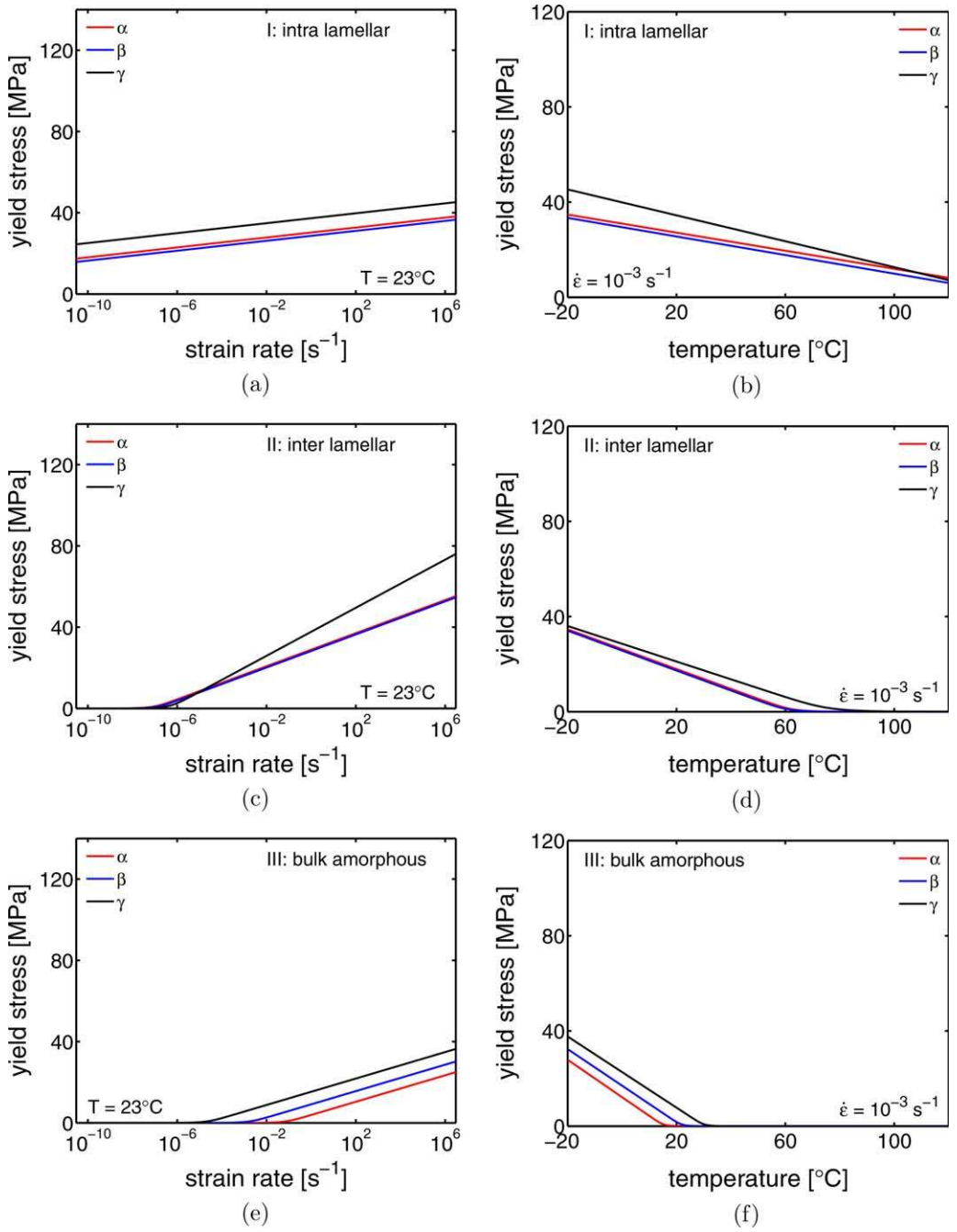

FIGURE 13 A comparison of the deformation mechanisms between the different crystallographic structures. Panels (a) and (b) show the rate and temperature dependence of process I, (c) and (d) show these dependencies for deformation mechanism II, and (e) and (f) show the same for mechanism III. [Color figure can be viewed at wileyonlinelibrary.com]

angle since chains are stretched perpendicular to the lamellae (also lamellar stacks with a different orientation will at some point rotate perpendicular to the deformation direction). This will hinder the diffuse crystal deformation and thus increase the resistance against yielding. The stress acting on the chain perpendicular to the lamellar stack can be decomposed in the following two parts: a component parallel to the chain and one perpendicular to the chain. The stress working parallel to the chain axis direction, that is, the stress required for diffuse crystal deformation, is a factor $\cos(40^{\circ})$ lower than the stress applied perpendicular to the lamellar stack. Remarkably, if we apply this same factor to the yield stress determined with the γ-iPP parameters, at high temperatures, where only deformation mechanism I contributes to the mechanical response, it follows that the yield stress is roughly the same as the ones found for α- and β-iPP. Instead, when comparing for example the yield stresses found at a strain rate of 10^{-2} and a temperature of 110 °C, values of

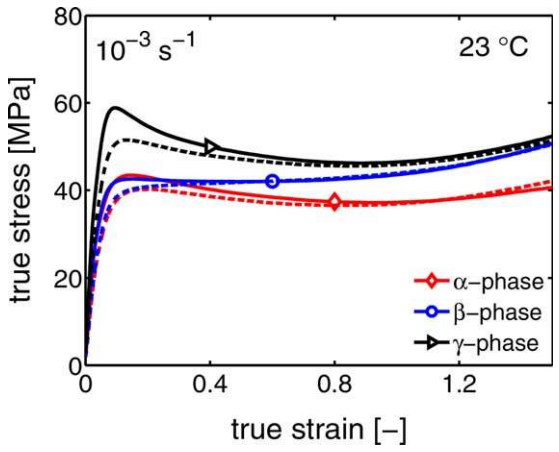

FIGURE 14 Intrinsic stress–strain response in uniaxial compression, taken at room temperature and a strain rate of 10^{-3} s^{-1}. The lines are the responses measured on the aged iPP and the dashed lines are measured on the rejuvenated iPP. [Color figure can be viewed at wileyonlinelibrary.com]

27.8, 26.2 and 26.7 MPa are found for α-, β- and γ-iPP, respectively. This confirms the hypothesis that the mobility of the helix within the crystal determines the deformation kinetics, rather than the crystal structure on its own. Nevertheless, the packing of the chain within the lattice seems to have a major influence on the level of the yield stress.

Besides a comparison based on the parameters used in the Eyring equation, differences and similarities in the three deformation mechanisms can also be visualized by plotting the contributions separately. In Figure 13(a,c,e), three distinct deformation mechanisms at room temperature are plotted for the α, β, and γ crystals. From these figures, it follows immediately that the strong stress dependence of γ-iPP (at low temperatures or high strain rates) in comparison with α- and β-iPP results from the inter-lamellar deformation mechanism and is therefore directly related to the constrained amorphous phase.

In order to compare the temperature dependence of each deformation mechanism similar plots are made and shown in Figure 13(b,d,f). In the intra-lamellar deformation mechanism the γ crystals display the strongest temperature dependence and the highest yield stress. Around a temperature of 120 °C, the descriptions coincide. Here, the γ and β crystals transform to the more stable monoclinic α- form[18,20] during deformation, and thus the model description does not hold at temperatures in this range. For the inter-lamellar deformation process it is found that the temperature dependence is the weakest for γ-iPP (smallest ΔU), however, if the effect of $\dot{\epsilon}_{0,II}$ is taken into account it appears that the mobility is the lowest, which might be explained with a higher amount of constraints on the amorphous regions in the vicinity of the crystal lattices. Finally, the bulk amorphous contribution shows a temperature dependence that intersects at 0 K, which is expected when the activation energy and volume are equal, as can be deduced from eq 7.

So far, all the mechanical analyses are performed on samples that had aged at room temperature for at least 1 month. In the intrinsic material response, a relation exists between the (aged) rigid amorphous fraction and the amount of softening, or the yield drop. Softening resulting from the glassy part is twofold: first, the yield drop depends on the age of rigid amorphous phase and, second, the amount or fraction of material in the rigid amorphous state also affects the softening. As a result, there is a clear relation between the age of the iPP and the yield kinetics below the α_c temperature. This is shown by Yue et al.[50] who investigated the effect of physical aging at room temperature. In their work, it is suggested that aging results in a decrease of the activation volume. To our knowledge, this effect has not been studied for β- or γ-iPP. In amorphous materials, the rate constant is typically the only state-dependent variable that is modified as a result of aging, although Senden et al. showed that in specific situations also the activation energy can increase with aging.[51,52] Modifying the rate factor of deformation mechanisms II and III, where physical aging can be observed, is therefore the most straightforward way to incorporate aging in the Eyring-based description.

Because of the above-mentioned effects, it makes sense to eliminate the contribution of aging and look at the mechanical properties of the rejuvenated iPP. In this study, a thermal treatment is used to rejuvenate the rigid amorphous fractions. The samples were first heated to 85 °C and kept there for 5 min to thermally rejuvenate, that is, mobilize, the constrained amorphous phase. After this, the samples were quenched in ice-water and tested immediately after. This treatment leaves the crystals unaffected and therefore enables us to look at effects in the amorphous contributions only. The result of the uniaxial compression experiments performed at room temperature and a strain rate of 10^{-3} S^{-1} are shown in Figure 14.

The effect of the rejuvenation treatment is particularly obvious for the γ-iPP, see Figure 14. The yield stress is much lower and the softening afterwards is less pronounced, hence the yield drop is much smaller. After softening, the hardening of the rejuvenated material coincides again with the hardening response of the aged iPP. This behavior is similar to that observed in amorphous polymers like polycarbonate and polystyrene.[53] The effect on the true stress - true strain of the α- and β-iPP is much smaller. However, both show a decrease in yield stress and the softening is less strong. Subsequently, the aged and rejuvenated material follows the same stress–strain response.

Yield Kinetics and Rejuvenation

Since the yield behavior is clearly affected by the rejuvenation treatment this will also be reflected in the kinetics. In order to reveal the changes, experiments on rejuvenated samples are performed. Figure 15 shows the deformation kinetics of the aged material (open markers) together with the yield stress resulting from rejuvenated samples. New Eyring parameters values are determined for the yield data

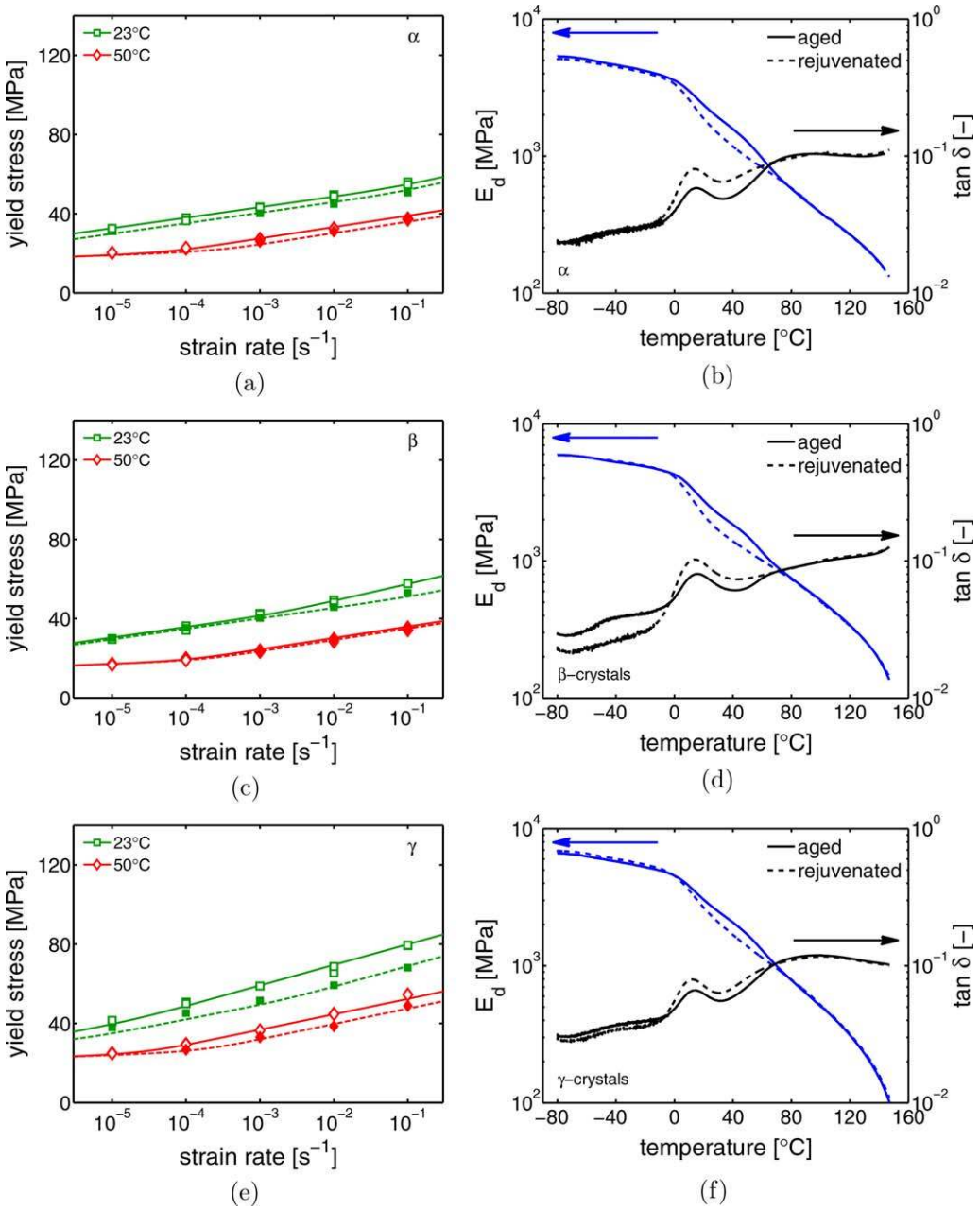

FIGURE 15 The yield kinetics of the iPP polymorphs for a range of temperatures. Open markers represent the yield stress obtained from aged iPP and solid markers are measured on rejuvenated material. Solid and dashed lines are Eyring descriptions of the aged and rejuvenated iPP respectively, for (a) α-iPP, (c) β-iPP, and (e) γ-iPP. The complex modulus and the *tan*(δ) of aged (solid lines) and rejuvenated (dashed lines) iPP containing (b) α, (d) β, and (f) γ crystals. [Color figure can be viewed at wileyonlinelibrary.com]

of process II, see Table 3, and the results are represented by the dashed lines in Figure 15. For the γ-iPP, the rate dependence becomes much less strong. This difference of γ-iPP with respect to α- and β-iPP can either be a result of the sample preparation procedure or it can be related to differences in aging kinetics. To model this, the rate constants of deformation mechanism II and III both have to be adapted. When looking at the new parameters values (Table 3) it indeed follows that with only a change in $\dot{\epsilon}_{0,II}$ and $\dot{\epsilon}_{0,III}$ the kinetics of the rejuvenated material at temperatures of 23 and 50 °C can be captured, as is illustrated in ref. 15 for all crystal structures. The temperature and rate dependence of the inter lamellar deformation mechanism for the rejuvenated samples is shown in Figure 16 and compared with that of the aged samples. As observed before, rejuvenation only leads to a shift in the rate and temperature at which the mechanisms become active. The decrease in yield stress seems to be inversely proportional to the amount of RAF.

TABLE 3 List of Parameter Values for the Rejuvenated Samples

	V_i^* [m^3]	ΔU_i [J·mol^{-1}]	$\dot{\epsilon}_{0,i}$ [s^{-1}]
α-Crystals			
Mechanism *I*	$7.70 \cdot 10^{-27}$	$3.84 \cdot 10^5$	$2.0 \cdot 10^{43}$
Mechanism *II*	$2.31 \cdot 10^{-27}$	$1.95 \cdot 10^5$	$2.0 \cdot 10^{28}$
Mechanism *III*	$2.89 \cdot 10^{-27}$	$3.95 \cdot 10^5$	$1.0 \cdot 10^{69}$
β-Crystals			
Mechanism *I*	$7.70 \cdot 10^{-27}$	$3.84 \cdot 10^5$	$4.2 \cdot 10^{44}$
Mechanism *II*	$2.31 \cdot 10^{-27}$	$1.95 \cdot 10^5$	$1.0 \cdot 10^{28}$
Mechanism *III*	$2.89 \cdot 10^{-27}$	$3.95 \cdot 10^5$	$1.6 \cdot 10^{68}$
γ-Crystals			
Mechanism *I*	$7.70 \cdot 10^{-27}$	$5.30 \cdot 10^5$	$2.0 \cdot 10^{63}$
Mechanism *II*	$1.59 \cdot 10^{-27}$	$1.25 \cdot 10^5$	$5.5 \cdot 10^{16}$
Mechanism *III*	$2.89 \cdot 10^{-27}$	$3.95 \cdot 10^5$	$9.0 \cdot 10^{66}$

DMTA

Finally, the rejuvenation is examined with DMTA experiments. Again the behavior of rejuvenated material is compared with that of aged iPP, see Figure 15(b,d,f). It immediately becomes clear that the biggest differences are observed in the temperature range of approximately 0–75 °C. This corresponds to the temperature window at which a distinction can be made between rigid and mobile amorphous domains, and is in good agreement with the work of Struik.[54] At lower temperatures, where the entire amorphous volume fraction is in a glassy state, and, at higher temperatures, where the amorphous material is completely in the mobile state, the complex modulus is equal for aged and rejuvenated samples. The $tan(\delta)$ at low temperatures has decreased in the case of the beta-iPP.

Failure Kinetics

In creep experiments, in which a constant load is applied and the resulting strain is measured, three creep regimes can be distinguished. First, the primary creep regime can be identified during which the strain increases with a decreasing plastic strain-rate. Subsequently, secondary creep will be observed. In this regime, the plastic strain rate is steady and accumulation of plastic strain takes place. Finally, in the tertiary creep regime, acceleration of plastic strain rate takes place results in the occurrence of failure. A set of typical results measured on α-iPP at room temperature is shown in Figure 17(a). The lines represent the creep curves, the red symbols mark the minimum in the plastic strain rate and the green markers indicate the time of failure, corresponding to a maximum in the strain rate. The determination of these points is done with a Sherby–Dorn plot, given in Figure 17(b). With increasing stress levels or temperatures, the accumulation of plastic strain is accelerated and thus failure takes place at shorter time scales. The strain at which the failure occurs, ϵ_f, is always in the order of 0.9 [-].

In the work of Bauwens-Crowet et al., it is shown that creep in the secondary regime is identical to the plastic flow in the yield point.[55] Since the mode of failure in the creep experiments is similar to the mode of failure in the constant strain rate experiments, the same kinetics will be followed. To illustrate that this holds also for experiments performed in this study, the applied stress of the creep experiments are plotted as a function of the plastic flow rates obtained from the Sherby–Dorn plots, Figure 18. The Eyring description (gray lines), used with the parameters determined on the constant rate experiments and given in Table 2, coincides with the creep data.

In order to use the Eyring equation to describe and predict the time to failure under a constant load, one can use the concept of critical strain. This concept is based on the observation that the plastic flow rate as a function of the applied stress, multiplied with the time to failure, is constant:

$$ttf(\sigma) \cdot \dot{\epsilon}_{pl}(\sigma) = C \tag{8}$$

This relation also holds for the experiments performed here. This is validated with Figure 19(a), which shows that the relation between the time to failure and the plastic flow rate is linear with a slope of -1 in a double logarithmic plot, that is, confirming eq 7.

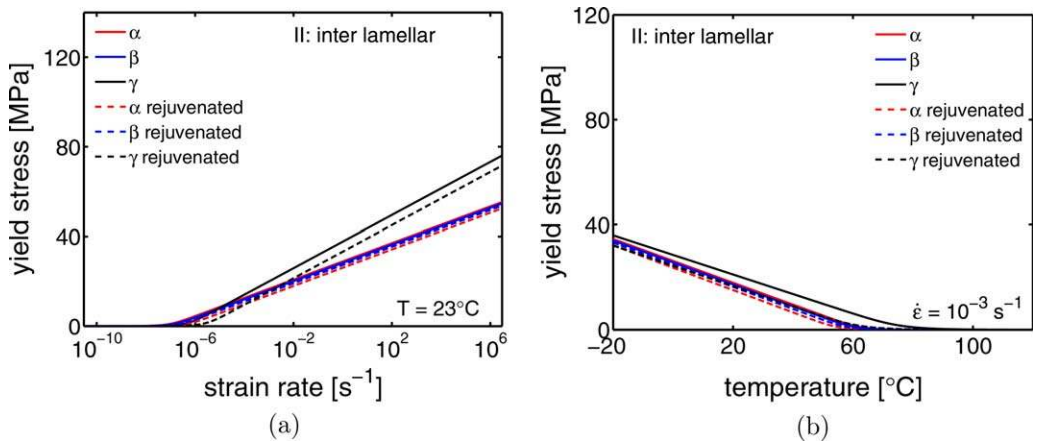

FIGURE 16 (a) The rate dependence of the interlamellar deformation mechanism and (b) the corresponding temperature dependence. [Color figure can be viewed at wileyonlinelibrary.com]

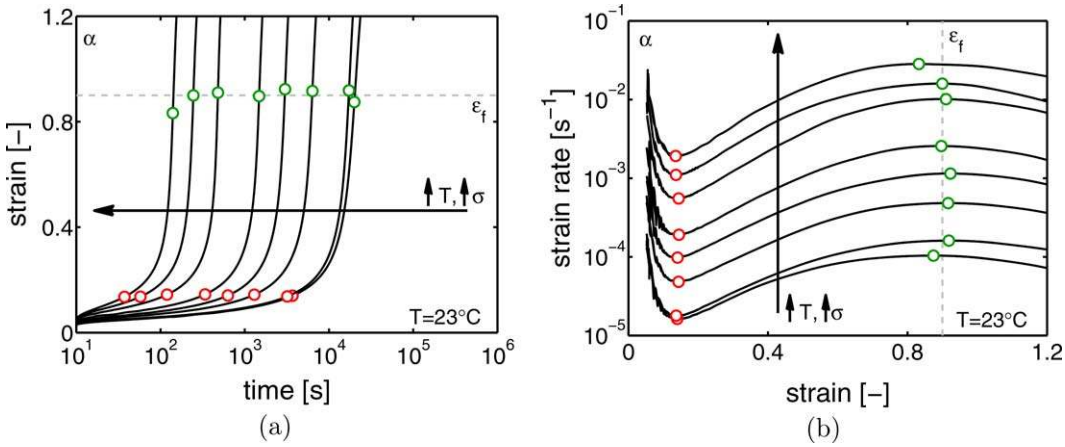

FIGURE 17 (a) The strain as a function of time under constant loading conditions. Markers indicate the minimal (red) and maximal plastic flow rate (green) in the creep experiment. (b) The accompanying Sherby–Dorn plot to illustrate the plastic flow rates for the set of creep experiments. [Color figure can be viewed at wileyonlinelibrary.com]

This constant C, can be visualized in a plot where the plastic strain, accumulated as a result of the applied stress, is plotted as a function of time (both on a linear scale), see Figure 19(b). This clarifies that the constant C is considered here as a critical strain ϵ_{cr}, which is different from the strain at failure ϵ_f. Making use of the fact that ϵ_{cr} is independent of the applied loading conditions [Fig. (19(b)] enables us to predict the time to failure according to:

$$ttf(\sigma, T) = \frac{\epsilon_{cr}}{\dot{\epsilon}_{pl}(\sigma, T)} \tag{9}$$

where ϵ_{cr} follows from the creep experiments and $\dot{\epsilon}_{pl}$ is the plastic strain rate. From this equation, it directly follows that at a time to failure of 1 s, $\epsilon_{cr}=\dot{\epsilon}_{pl}$, the value of the critical strain equals the one of the plastic flow rate indicated with the dashed line in Figure 19(a). For a given stress, the plastic flow rate $\dot{\epsilon}_{pl}$ follows directly from the Eyring equation, using the parameters given in Table 2. Application of this concept is straightforward in the case of the α and γ crystals. However, in the case of β-iPP, the Sherby–Dorn plots do not always display a minimum and/or maximum. Based on the creep experiments performed at lower temperatures, where there was a clear minimum and maximum, the plastic strain rate was determined at a true strain of 0.2 [-] and the time to failure at a true strain ϵ_f of 0.4 [-]. The critical strain ϵ_{cr} used to describe the creep data of all the crystallographic structures is 0.24 [-].

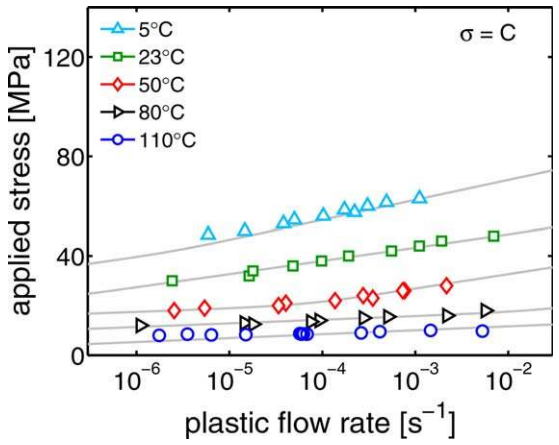

FIGURE 18 The applied stress of α-iPP is plotted as a function of the plastic strain rate for different temperatures. Lines are model descriptions using the parameters given in Table 2 substituted into eq 7. [Color figure can be viewed at wileyonlinelibrary.com]

When applying eq 9, the predictions shown in Figure 20 are obtained. The markers in these figures are the result of the creep experiments and the match proofs the validity of the concept of critical strain. For all loads and temperatures, excellent agreement is found, except for the creep experiments performed at 110 °C. For these experiments, increasing deviations can be found upon longer times to failure. It is likely that this deviation is caused by structural evolution (annealing), which increases the yield stress as a result of the applied temperature and stress level within the experimental time scale.

CONCLUSION

To study the performance of iPP polymorphs different sample preparation procedures are used on an injection molding iPP grade. It is shown that these protocols result in samples containing almost solely the monoclinic α-, the pseudo-hexagonal β- or the orthorhombic γ-crystal unit cell structure and therefore allow to study their mechanical response. A comparison of the intrinsic material response shows that:

- The γ samples have the highest modulus and the α samples have the lowest. Although differences in crystallinity are small, it is assumed to partially cause the differences in the Young's modulus. The other contribution to the modulus follows from the part of the amorphous phase in the glassy state (RAF) and, therefore, is directly related to the constraints imposed by the crystals.

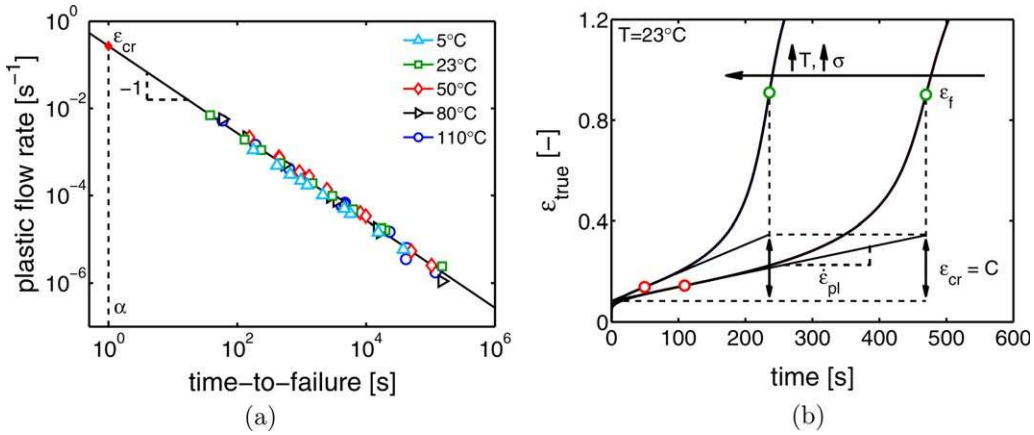

FIGURE 19 (a) The plastic flow rate as a function of the time to failure on a logarithmic scale. The open markers represent the temperatures at which the creep experiments were performed, and the filled marker is the critical strain. (b) Creep curves of samples subjected to different loads to illustrate the effect of loading conditions. Furthermore, the definition of the critical strain and the strain at failure is indicated. [Color figure can be viewed at wileyonlinelibrary.com]

- The level of the yield stress turns out to be very similar for the α-crystals and the β-crystals (for the whole range in temperature and strain rate), even though significant differences in lamellar thickness are found. The γ-crystals show a yield stress level which is clearly higher. It is therefore plausible that besides crystallinity (similar for all three samples) and lamellar thickness (β much higher than α- and γ-iPP) the chain packing within the crystal lattice contributes to the magnitude of the yield stress. Moreover, the constraints of the amorphous chains in the vicinity of the

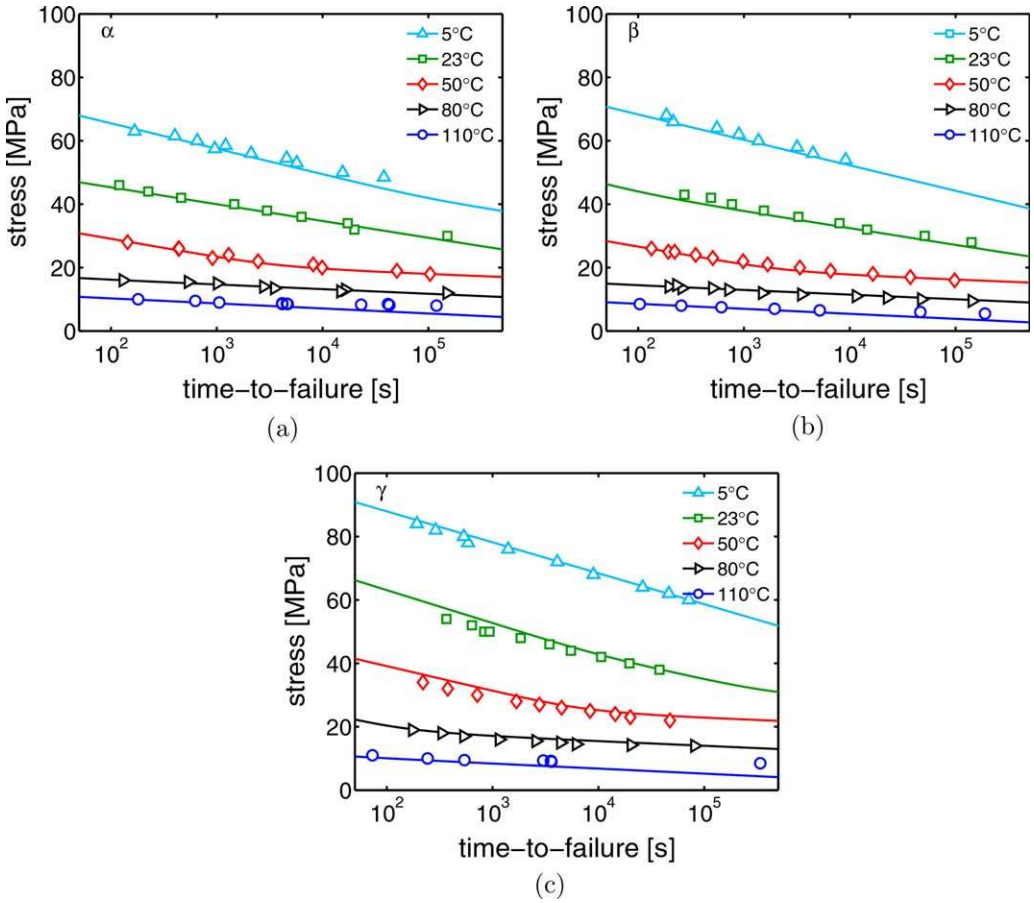

FIGURE 20 Time to failure as a function of the applied load for different temperatures of (a) α-iPP, (b) β-iPP, and (c) γ-iPP. The lines are the predictions based on the concept of critical strain and the Eyring theory and the markers represent experimentally obtained creep data. [Color figure can be viewed at wileyonlinelibrary.com]

crystals have significant influence on the yield stress and appear to be the strongest for γ-iPP.
- Softening after yielding is linked to the thermodynamic state of the rigid amorphous fraction and was the most pronounced for γ-crystals, whereas β-iPP showed no softening. This observation fits the hypothesis that γ crystals impose the largest constraints on the amorphous phase and suggests that constraints imposed by β crystals are relatively weak.
- Hardening of the β samples was much stronger compared to the α and γ samples. In this work, no direct factors or structural features were found that could be on the basis of this observation. However, it is expected that further research into the structural evolution upon deformation could explain the results.

The performance under various loading conditions of iPP, containing one of the polymorphs, is also investigated. It is remarkably found that the yield kinetics in the intralamellar deformation regime (at high temperatures and/or low strain rates) are the same for all three samples in terms of activation volume. This could be an indication that the kinetics of this deformation mechanism are determined by the mobility of the 3/1 helix, rather than the crystal slip systems. The high activation energy of γ-iPP with respect to α- and β-iPP is hypothetically explained by taking the angle of the chains with respect to the lamellar surface in γ-crystals into account.

In the interlamellar deformation regime, which contributes at temperatures where the rigid amorphous fraction is present in the vicinity of the crystals, γ-iPP has the highest resistance against yielding. Rejuvenation of the samples yields a decrease in the yield stress which is particularly strong in γ-iPP. This is matches with the above mentioned findings with respect to softening, and illustrates that the constrained amorphous fraction is a very important factor affecting the yield stress (hence, the crystals remain unaffected by the rejuvenation treatment). The contribution of the bulk amorphous phase to the yield kinetics, observed at low temperatures, can be described with the same activation volume and energy for all three samples.

To predict the time to failure as a function of applied stress and temperature, the concept of critical stain is successfully used. It is shown that the same critical strain can be used for all three crystals. It is predicted that, in the plasticity-controlled failure regime, the performance of γ-iPP is better than that of α- and β-iPP. The predictions were validated with experimental results obtained from creep experiments and match very well. At high temperature and long testing times, a deviation is found between the predictions and the experiments, probably caused by structural changes of the samples.

ACKNOWLEDGMENTS

The authors thank SABIC for the financial support and Rieky Steenbakkers and Klaas Remerie for the valuable discussions throughout this study. The staff of DUBBLE (beamline 26 The European Synchrotron and Radiation facility) is acknowledged for their assistance in the wide and small-angle X-ray experiments. Furthermore, R. Di Girolamo is acknowledged for providing the schematics of the different polymorphic structures.

REFERENCES AND NOTES

1 M. Kristiansen, M. Werner, T. Tervoort, P. Smith, M. Blomenhofer, H. W. Schmidt, *Macromolecules* **2003**, *36*, 5150–5156.

2 Z. Horváth, A. Menyhárd, P. Doshev, M. Gahleitner, G. Vörös, J. Varga, B. Pukánszky, *ACS Appl. Mater. Interfaces* **2014**, *6*, 7456–7463.

3 F. Luo, K. Wang, N. Ning, C. Geng, H. Deng, F. Chen, Q. Fu, Y. Qian, D. Zheng, *Polym. Adv. Technol.* **2011**, *22*, 2044–2054.

4 K. H. Nitta, Y. W. Shin, H. Hashiguchi, S. Tanimoto, M. Terano, *Polymer* **2005**, *46*, 965–975.

5 C. De Rosa, F. Auriemma, *Polym. Chem.* **2011**, *2*, 2155–2168.

6 M. Naffakh, Z. Martín, N. Fanegas, C. Marco, M. A. Gómez, I. Jiménez, *J. Polym. Sci. Part B: Polym. Phys.* **2007**, *45*, 2309–2321.

7 T. B. Van Erp, D. Cavallo, G. W. M. Peters, L. E. Govaert, *J. Polym. Sci. Part B: Polym. Phys.* **2012**, *50*, 1438–1451.

8 S. V. Meille, D. R. Ferro, S. Brückner, A. J. Lovinger, F. J. Padden, *Macromolecules* **1994**, *27*, 2615–2622.

9 B. Lotz, J. C. Wittmann, A. J. Lovinger, *Polymer* **1996**, *37*, 4979–4992.

10 K. Mezghani, P. J. Phillips, *Polymer* **1998**, *39*, 3735–3744.

11 C. D. Rosa, F. Auriemma, A. D. Capua, L. Resconi, S. Guidotti, I. Camurati, I. E. Nifant'ev, I. P. Laishevtsev, *J. Am. Chem. Soc.* **2004**, *126*, 17040–17049.

12 S. Valdo Meille, S. Brückner, *Nature* **1989**, *340*, 455–457.

13 J. Varga, J. Karger-Kocsis, *J. Polym. Sci. Part B: Polym. Phys.* **1996**, *34*, 657–670.

14 J. Varga, I. Mudra, G. W. Ehrenstein, *J. Appl. Polym. Sci.* **1999**, *74*, 2357–2368.

15 C. De Rosa, F. Auriemma, R. Di Girolamo, O. R. De Ballesteros, M. Pepe, O. Tarallo, A. Malafronte, *Macromolecules* **2013**, *46*, 5202–5214.

16 D. Cavallo, F. Azzurri, R. Floris, G. C. Alfonso, L. Balzano, G. W. Peters, *Macromolecules* **2010**, *43*, 2890–2896.

17 E. Lezak, Z. Bartczak, A. Galeski, *Polymer* **2006**, *47*, 8562–8574.

18 E. Lezak, Z. Bartczak, *J. Polym. Sci. Part B: Polym. Phys.* **2008**, *46*, 92–108.

19 W. Xu, D. C. Martin, E. M. Arruda, *Polymer* **2005**, *46*, 455–470.

20 E. Lezak, Z. Bartczak, A. Galeski, *Macromolecules* **2006**, *39*, 4811–4819.

21 F. Auriemma, C. D. Rosa, *Macromolecules* **2006**, *39*, 7635–7647.

22 B. Na, R. Lv, W. Xu, *J. Appl. Polym. Sci.* **2009**, *113*, 4092–4099.

23 R. Thomann, H. Semke, R. D. Maier, Y. Thomann, J. Scherble, R. Mülhaupt, J. Kressler, *Polymer* **2001**, *42*, 4597–4603.

24 W. Bras, I. P. Dolbnya, D. Detollenaere, R. Van Tol, M. Malfois, G. N. Greaves, A. J. Ryan, E. Heeley, *J. Appl. Crystallogr.* **2003**, *36*, 791–794.

25 M. Van Drongelen, T. B. Van Erp, G. W. M. Peters, *Polymer* **2012**, *53*, 4758–4769.

26 R. H. Boyd, *Polymer* **1985**, *26*, 1123–1133.

27 C. Hedesiu, D. E. Demco, R. Kleppinger, G. V. Poel, K. Remerie, V. M. Litvinov, B. Blümich, R. Steenbakkers, *Macromol. Mater. Eng.* **2008**, *293*, 847–857.

28 Q. Zia, D. Mileva, R. Androsch, *Macromolecules* **2008**, *41*, 8095–8102.

29 O. Policianová, J. Hodan, J. Brus, J. Kotek, *Polymer (United Kingdom)* **2015**, *60*, 107–114.

30 M. P. F. Pepels, L. E. Govaert, R. Duchateau, *Macromolecules* **2015**, *48*, 5845–5854.

31 H. J. M. Caelers, L. E. Govaert, G. W. M. Peters, *Polymer (United Kingdom)* **2016**, *83*, 116–128.

32 R. Thomann, C. Wang, J. Kressler, R. Muelhaupt, *Macromolecules* **1996**, *29*, 8425–8434.

33 B. A. G. Schrauwen, R. P. M. Janssen, L. E. Govaert, H. E. H. Meijer, *Macromolecules* **2004**, *37*, 6069–6078.

34 P. Zhang, X. Liu, Y. Li, *Mater. Sci. Eng. A* **2006**, *434*, 310–313.

35 C. Zhang, G. Liu, Y. Song, Y. Zhao, D. Wang, *Polymer (United Kingdom)* **2015**, *55*, 6915–6923.

36 Z. Ma, C. Shao, X. Wang, B. Zhao, X. Li, H. An, T. Yan, Z. Li, L. Li, *Polymer* **2009**, *50*, 2706–2715.

37 F. Zuo, J. K. Keum, X. Chen, B. S. Hsiao, H. Chen, S. Y. Lai, R. Wevers, J. Li, *Polymer* **2007**, *48*, 6867–6880.

38 C. Bauwens-Crowet, J. C. Bauwens, G. Homès, *J. Polym. Sci. Part A-2: Polym. Phys.* **1969**, *7*, 735–742.

39 J. A. Roetling, *Polymer* **1966**, *7*, 303–306.

40 T. Ree, H. Eyring, *J. Appl. Phys.* **1955**, *26*, 793–800.

41 R. W. Truss, P. L. Clarke, R. A. Duckett, I. M. Ward, *J. Polym. Sci. Part A-2: Polym. Phys.* **1984**, *22*, 191–209.

42 L. E. Govaert, P. J. De Vries, P. J. Fennis, W. F. Nijenhuis, J. P. Keustermans, *Polymer* **2000**, *41*, 1959–1962.

43 K. Schmidt-Rohr, H. W. Spiess, *Macromolecules* **1991**, *24*, 5288–5293.

44 G. Attalla, I. B. Guanella, R. E. Cohen, *Polym. Eng. Sci.* **1983**, *23*, 883–887.

45 T. Ariyama, Y. Mori, K. Kaneko, *Polym. Eng. Sci.* **1997**, *37*, 81–90.

46 R. J. Young, *Mater. Forum* **1988**, *11*, 210–216.

47 M. J. W. Kanters, K. Remerie, L. E. Govaert, *Polym. Eng. Sci.* **2016**, *56*, 676–688.

48 A. Sedighiamiri, L. E. Govaert, M. J. W. Kanters, J. A. W. Van Dommelen, *J. Polym. Sci. Part B: Polym. Phys.* **2012**, *50*, 1664–1679.

49 W. G. Hn, K. Schmidt-Rohr, *Acta Polym.* **1999**, *50*, 271–285.

50 C. Y. Yue, W. F. Msuya, *J. Mater. Sci. Lett.* **1990**, *9*, 985–988.

51 L. E. Govaert, T. A. P. Engels, E. T. J. Klompen, G. W. M. Peters, H. E. H. Meijer, *Int. Polym. Process.* **2005**, *20*, 170–177.

52 D. J. A. Senden, J. A. W. Van Dommelen, L. E. Govaert, *J. Polym. Sci. Part B: Polym. Phys.* **2012**, *50*, 1589–1596.

53 H. E. H. Meijer, L. E. Govaert, *Prog. Polym. Sci. (Oxford)* **2005**, *30*, 915–938.

54 L. C. E. Struik, *Polymer* **1987**, *28*, 1534–1542.

55 C. Bauwens-Crowet, J. M. Ots, J. C. Bauwens, *J. Mater. Sci.* **1974**, *9*, 1197–1201.